Advanced Functional Materials

ADVANCED FUNCTIONAL MATERIALS
www.afm-journal.de

RESEARCH ARTICLE

All-In-One Flexible Thermoelectric Yarns for Integrated Energy Harvesting, Adaptive Personal Thermal Management, and Self-Powered Sensing

Haoran Yu[1] | Dequan Sun[1,3] | Wenbo Dong[1] | Ruirui Cao[1,2] | Yuqing Zhou[1] | Yujun Zhang[4] | Le Li[1] | Binchuan Cao[1] | Jidong Shi[1] | Jiaxin Yu[1] | Caofeng Pan[2]

[1]Henan Key Laboratory of Quantum Materials and Quantum Energy, School of Future Technology, Henan University, Kaifeng, China | [2]Institute of Atomic Manufacturing, International Research Institute For Multidisciplinary Science, Beihang University, Beijing, China | [3]School of Material Science and Engineering, Tiangong University, Tianjin, China | [4]Department of Urology & Andrology, Sir Run Run Shaw Hospital, Zhejiang University School of Medicine, Hangzhou, China

Correspondence: Ruirui Cao (rrcao0403@vip.henu.edu.cn) | Caofeng Pan (pancaofeng@buaa.edu.cn)

Received: 22 September 2025 | **Revised:** 10 November 2025 | **Accepted:** 24 November 2025

Keywords: energy-harvesting | multifunctional integration | personal thermal management | self-powered sensor | thermoelectric yarn

ABSTRACT

Wearable thermoelectric generators (TEGs) offer a sustainable pathway to power emerging electronics by harvesting body heat, yet their practical adoption is hindered by limited energy conversion efficiency and poor thermal comfort. To overcome these restrictions, we herein develop stretchable thermo-regulated TE yarns (STRTEYs) via coaxial electrospinning coupled with coagulation-bath wet spinning. The resulting shell-core nanofiber based STRTEYs exhibit high flexibility (>35%), excellent adaptive phase-change PTM (110 J/g), long-term stability and enhanced TE performance (σ of 32 S/cm, S of 46 μV/K). Noteworthy, through efficient latent heat management, the STRTEYs achieve an exceptional ≈393 s extension in effective TE output duration, demonstrating remarkable synergy between PTM and energy harvesting. Furthermore, the STRTEYs maintained stable TE property (S = 45.85 μV/K) after 5-month storage and notably enhanced TE output via temperature difference stability. The mask integrated with STRTEYs can achieve thermal energy collection and self-powered real-time detection of physiological signals. In summary, the STRTEYs successfully achieved efficient integration of multiple functions including energy harvesting, adaptive PTM, and self-powered sensing, providing a new research direction for developing advanced multifunctional TEGs and promoting their application in wearable electronics.

1 | Introduction

Portable devices integrated with sensors enable remote and sustainable monitoring and early-warning, addressing the critical demands for human health information collection and physical activity monitoring while advancing the development of the Internet of Things (IoT) [1–4]. However, the escalating power consumption of multifunctional sensors conflicts with the unsurpassable physical limitations of current battery technology [5]. This mismatch compels wearable devices to undergo frequent recharging or battery replacement, disrupting continuous data acquisition [6, 7]. Thermoelectric (TE) materials offer a groundbreaking solution through direct thermal-to-electrical energy transduction via the Seebeck effect, making them ideal for

Haoran Yu, Dequan Sun, and Wenbo Dong contributed equally to this work.

manufacturing TE generators (TEGs) with long lifespans, small sizes, noise-free operation, and extremely low maintenance requirements [5, 8]. Wearable TEGs capitalize on this by harvesting body heat to reliably power low-power sensors, significantly reducing battery dependence and advancing self-powered electronic devices [9–11]. This establishes a technological pillar for the realization of energy interconnection and the Internet of Everything.

For TEGs, their theoretical maximum thermoelectric conversion efficiency (η_{TEG}) can be estimated through Equations (1) and (2) [12, 13]:

$$\eta_{TEG}(\Delta T) = \frac{\Delta T}{T_h} \times \frac{\sqrt{1+ZT} - 1}{\sqrt{1+ZT} + \frac{T_c}{T_h}} \quad (1)$$

$$ZT = \frac{\sigma S^2 T}{k} \quad (2)$$

where σ (electrical conductivity, S/m), S (Seebeck coefficient, μV/K), k (thermal conductivity, W/(m·K)), ZT (thermoelectric figure of merit), T_h (hot-side temperature,°C), T_c (cold-side temperature,°C), ΔT (temperature gradient,°C), and T (absolute temperature, K) define the material's TE performance [14]. As indicated by the formulas, maximizing TE performance requires a synergistic optimization of the power factor ($PF = \sigma S^2$) and a reduction of k to enhance the ZT. For devices, a large ΔT is critical for high output [15]. Despite their inherent reliability and eco-friendly solid-state operation, the development and widespread application of wearable TEGs is hindered by inadequate conversion efficiency and thermal comfort issues [16–19]. These challenges underscore the imperative to develop efficient wearable TEG devices equipped with integrated personal thermal management (PTM) functionality [20]. Advanced PTM strategies aim to amplify ΔT through dynamic heat flux regulation while maintaining thermal comfort, thus augmenting both energy conversion efficiency and long-term wearability—a dual optimization essential for practical deployment in self-powered healthcare monitoring and IoT ecosystems.

PTM technology optimizes individualized thermal comfort by dynamically regulating the body-clothing-environment microclimate offering a sustainable path to reduce energy consumption [21, 22]. Phase change materials (PCMs), with their high latent heat capacity and quasi-isothermal phase transition behavior, provide adaptive temperature regulation capability [23–25]. As the "second skin" [26], textiles are ideal platforms for integrating PCMs, which not only confer adaptive bidirectional temperature regulation abilities but also enhance the output performance of integrated TE devices [27–31]. For instance, Yuan et al. demonstrated a 2.6-fold increase in open-circuit voltage (90.8 mV) by introducing high thermal/electrical conductivity PCMs into a solar-driven TE array [32]. Similarly, He et al. prepared a multifunctional phase-change organohydrogel that efficiently collects and transfers waste heat to significantly improve TE conversion efficiency [33]. Therefore, the strategic integration of PCMs into textile-based TEGs is essential to sustain substantial thermal gradients, amplify power output, and ensure long-term wearability. By leveraging the dual functions of PCMs—adaptive latent heat storage and release for ΔT stabilization and thermal buffering to mitigate interfacial heat accumulation—these systems address the critical trade-off between energy harvesting efficiency and thermal comfort. Nevertheless, research on PCM-embedded PTM textiles for synergistically optimizing both TE performance and thermal comfort of wearable TEGs remains nascent.

Based on current research status, this study focuses on the development of PCM-based stretchable adaptive thermo-regulated TE yarns (STRTEYs). As shown in Figure 1, we employed *n*-octadecane (*n*-OD) with exceptional thermal storage and temperature regulation properties as the phase-change functional component, single-walled carbon nanotubes (SWCNT) and PEDOT:PSS as the TE functional components, while robust polyurethane (PU) as the substrate. Through a combined process of coaxial electrospinning and coagulation bath wet spinning, a core-shell nanofiber-based STRTEYs with high flexibility (>35%), superior adaptive thermo-regulated performance (enthalpy value approximately 110 J/g, cooling capacity of 5.1 °C (vs. pure PU yarn) and 4.3 °C (vs. control yarn), insulation capacity of 5.1 °C (vs. pure PU yarn) and 4.7 °C (vs. control yarn)), and enhanced TE properties (σ of 32 S/cm, S of 46 μV/K) was successfully prepared. After a 5-month storage, the STRTEYs still maintained stable TE property ($S = 45.85$ μV/K), exhibiting long-term stability. More importantly, the STRTEYs not only ensure the long-term thermal comfort of wearable TEG devices but also improve the TE conversion efficiency by optimizing the stability of the temperature difference, achieving the synergistic optimization of PTM and efficient TE energy harvesting. A prototype respiratory-monitoring face mask integrated with STRTEYs demonstrated its ability to human energy harvesting and self-powered real-time monitoring of physiological signals. In summary, the STRTEYs effectively achieve efficient integration of functions including energy harvesting, adaptive PTM, and self-powered sensing, which establishes a new paradigm for multifunctional thermoelectric systems, propelling self-powered wearable devices toward the goal of "zero-energy thermal comfort".

2 | Experimental Section

2.1 | Materials

PU (1185A, BASF), poly(ethyleneimine) (PEI, 99%, Aladdin), *N,N*-dimethylformamide (DMF, AR, Aladdin), SWCNT (TNS, TimesNano), PEDOT:PSS (1.3 wt.%, Sigma-Aldrich), *n*-OD (98%, Aladdin), and kerosene (Aladdin) were used as received.

2.2 | Preparation of Thermo-Regulated Shell-Core Nanofiber Films (SCNFs)

A series of SCNF samples were prepared via coaxial electrospinning, employing a PU/PEI/DMF mixed solution with a mass ratio of 26:0.5:73.5 as the shell-layer spinning solution and an *n*-OD/kerosene mixed solution with an 80 wt.% *n*-OD content as the core-layer spinning solution. The shell-layer flow rate was fixed at 1 mL/h, while the core-layer flow rate was varied in a gradient of 0.5, 0.7, 0.9, 1.0, and 1.1 mL/h, resulting in

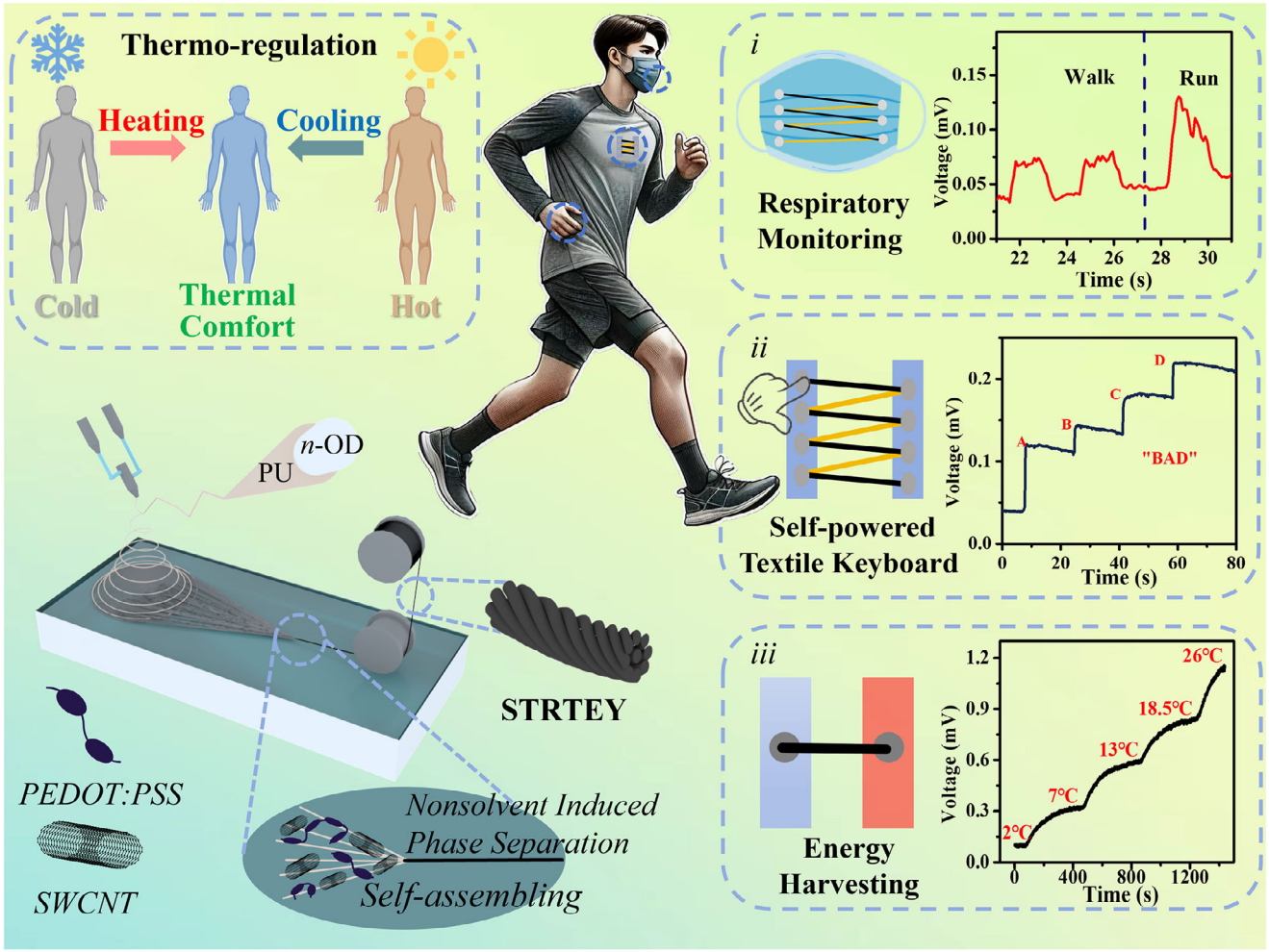

FIGURE 1 | Schematic illustration of the fabrication process, structural architecture, and operational mechanism of multifunctional STRTEYs.

corresponding samples sequentially labeled as SCNF1 to SCNF5. The electrospinning parameters were set as follows: a voltage of 12 kV, a receiving distance of 20 cm, with relative humidity and temperature controlled at 40 ± 5% and 30 ± 5°C, respectively.

2.3 | Preparation of STRTEYs

A 300 mL DMF/H_2O mixture (7:3, v/v) was employed as the base matrix. SWCNT and PEDOT:PSS, with a cumulative solid mass of 600 mg, were added in varying mass ratios, followed by 3 h of probe sonication at 600 W to yield a homogeneous dispersion, which acted as the coagulation bath. A series of STRTEY samples were synthesized via a coagulation bath-integrated coaxial electrospinning technique, as displayed in Figure 1 and Video S1. The formulations and feed rates (1 mL/h) of the shell and core spinning solutions adhered to those used in prior experiments. The SWCNT-to-PEDOT:PSS mass ratios in the coagulation bath were systematically adjusted to 2:8, 4:6, 6:4, and 8:2, corresponding to samples designated STRTEY1 to STRTEY4. The electrospinning parameters included a 10 kV voltage, a 3 cm tip-to-bath distance, and a rotating winding roller was utilized as the yarn collection device, with the coagulation bath grounded to ensure process stability.

2.4 | Characterization

Field-emission scanning electron microscopy (SEM, JSM-7001F, JEOL, Japan) was employed to analyze the surface and cross-section morphologies of SCNFs and STRTEYs, with the Nano Measure software utilized to extract diameter distributions from SEM images. ATR-FTIR spectroscopy (VERTEX 70, Bruker, Germany) was applied to characterize the chemical structures of these samples. Differential scanning calorimetry (DSC250, TA Instruments, USA) and thermogravimetric analyzer (TGA/DSC3+, Mettler Toledo, Switzerland) were conducted to evaluate the thermo-regulated characteristic and thermal stability of the above samples, operating at a heating/cooling rates of ±10°C/min and a heating rate of 10°C/min, respectively. The thermal regulation capacity was characterized by using an infrared thermal imager (E6-XT, FLIR, USA) and a multi-channel temperature measurement system (IV3000, IVYTECH). To establish simulated thermal environments and heating/cooling conditions, a hot plate maintained at approximately 40°C and a sealed ice bag at around 0°C were employed as the thermal source and cooling source, respectively. The Seebeck coefficient of STRTEYs was measured by a self-made test system. The real-time thermovoltage output and resistance of STRTEYs were measured by a multimeter (Keithley 2450).

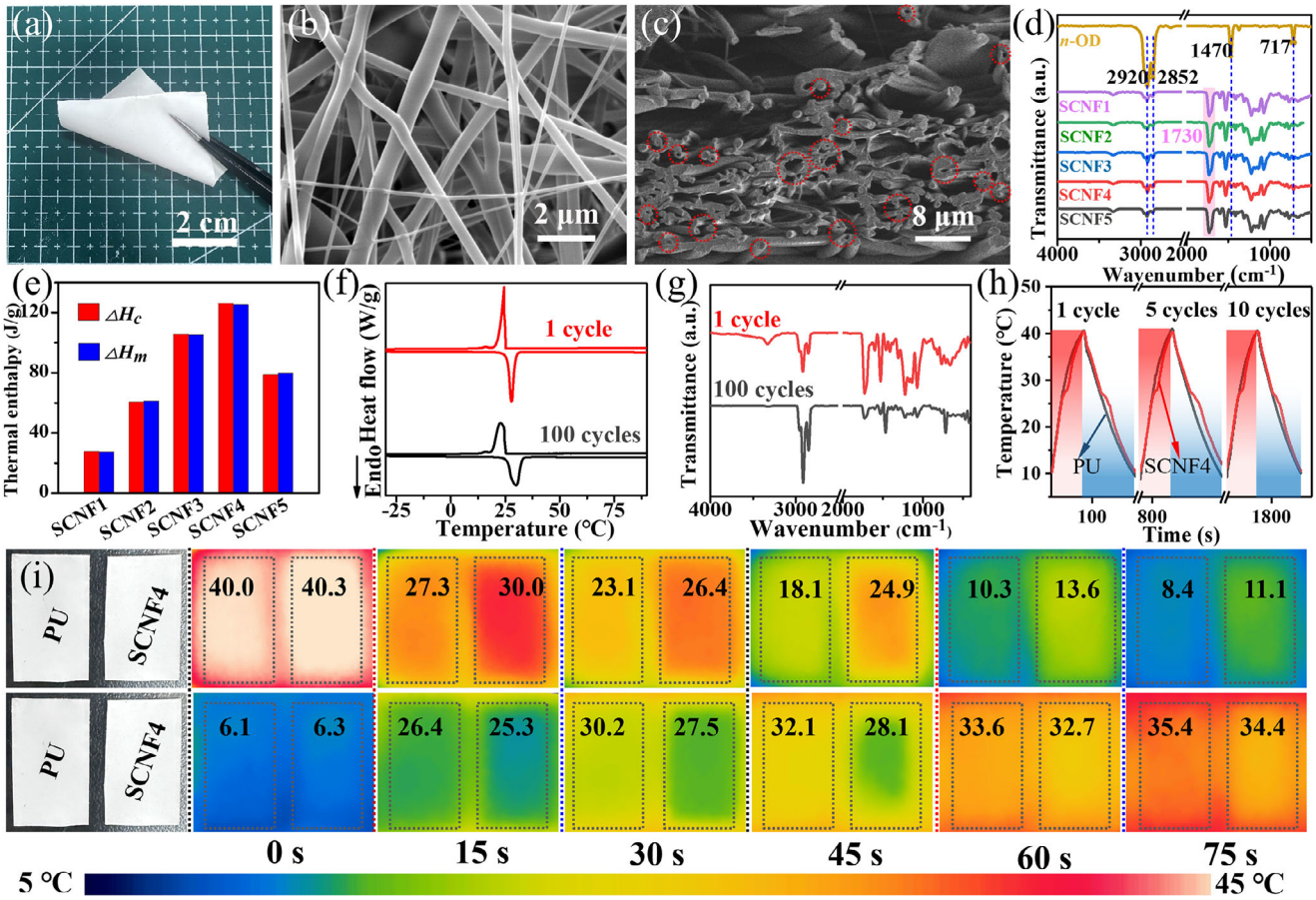

FIGURE 2 | (a) Optical photograph of SCNF4. (b) Surface and (c) cross-section SEM images of SCNF4. (d) FTIR spectra of *n*-OD and SCNFs. (e) Enthalpy of SCNFs during the melting and crystallization stages. (f) FTIR spectra and (g) DSC curves of SCNF4 before and after 100 thermal cycles. (h) Temperature-time curves of pure PU nanofiber film and SCNF4 after 10 thermal cycles. (i) Infrared thermal images of PU and PSCNF4 during cooling (up) and heating (down) process.

3 | Results and Discussion

As previously discussed, designing textile-based TEGs that integrate latent heat storage and thermal buffering capabilities is crucial for maintaining a substantial ΔT between the hot and cold ends of TE modules, enhancing output efficiency, and ensuring long-term thermal comfort for wearable TEGs [34–36]. Based on this premise, as illustrated in Figure 1, this study employed *n*-OD as the thermo-regulated functional component, owing to its exceptional latent heat storage/release and adaptive temperature regulation properties [37], with a phase-transition temperature that aligns with the human comfort temperature range [23, 38]. SWCNT and PEDOT:PSS were utilized as the TE functional components due to their complementary advantages and synergistic effects [39–42]. PEDOT:PSS, a widely studied conductive polymer, offers excellent solution processability, mechanical flexibility, and low thermal conductivity, serving as an ideal matrix for flexible TE systems. SWCNTs contribute high electrical conductivity, a large specific surface area, and a well-defined one-dimensional structure, which collectively promotes the formation of efficient charge transport pathways and induce energy-filtering effects at the interfaces. The strong π-π interactions between PEDOT chains and SWCNTs further enhance carrier transport, leading to a simultaneous increase in both electrical conductivity and Seebeck coefficient. Meanwhile, PU, renowned for its excellent flexibility, served as the substrate. The continuous yarn formation process, visually documented in Video S1, involves coaxial electrospinning of core-sheath spinning solutions into an aqueous coagulation bath containing SWCNT/PEDOT:PSS dispersion. During deposition, non-solvent induced phase separation occurs between DMF and water, while electrostatic self-assembly between cationic PEI and anionic PSS enables stable incorporation of TE materials within individual nanofibers. The resulting nanofibers are continuously drawn and twisted into aligned yarns by rotational winding, effectively converting the electrospun film into a mechanically robust yarn architecture. This integrated approach ensures internal encapsulation of TE components rather than surface coating, significantly enhancing interfacial stability. As a result, by leveraging a coupled process of coaxial electrospinning and wet spinning in a coagulation bath, we successfully fabricated multifunctional TE yarns that seamlessly integrate energy harvesting, adaptive PTM, and self-powered sensing capabilities. The scalable coagulation bath-assisted coaxial electrospinning technique employed in this process not only robustly encapsulates the *n*-OD within the PU shell, effectively mitigating leakage risks during application, but also imparts superior mechanical properties such as flexibility and stretchability to the TE yarns.

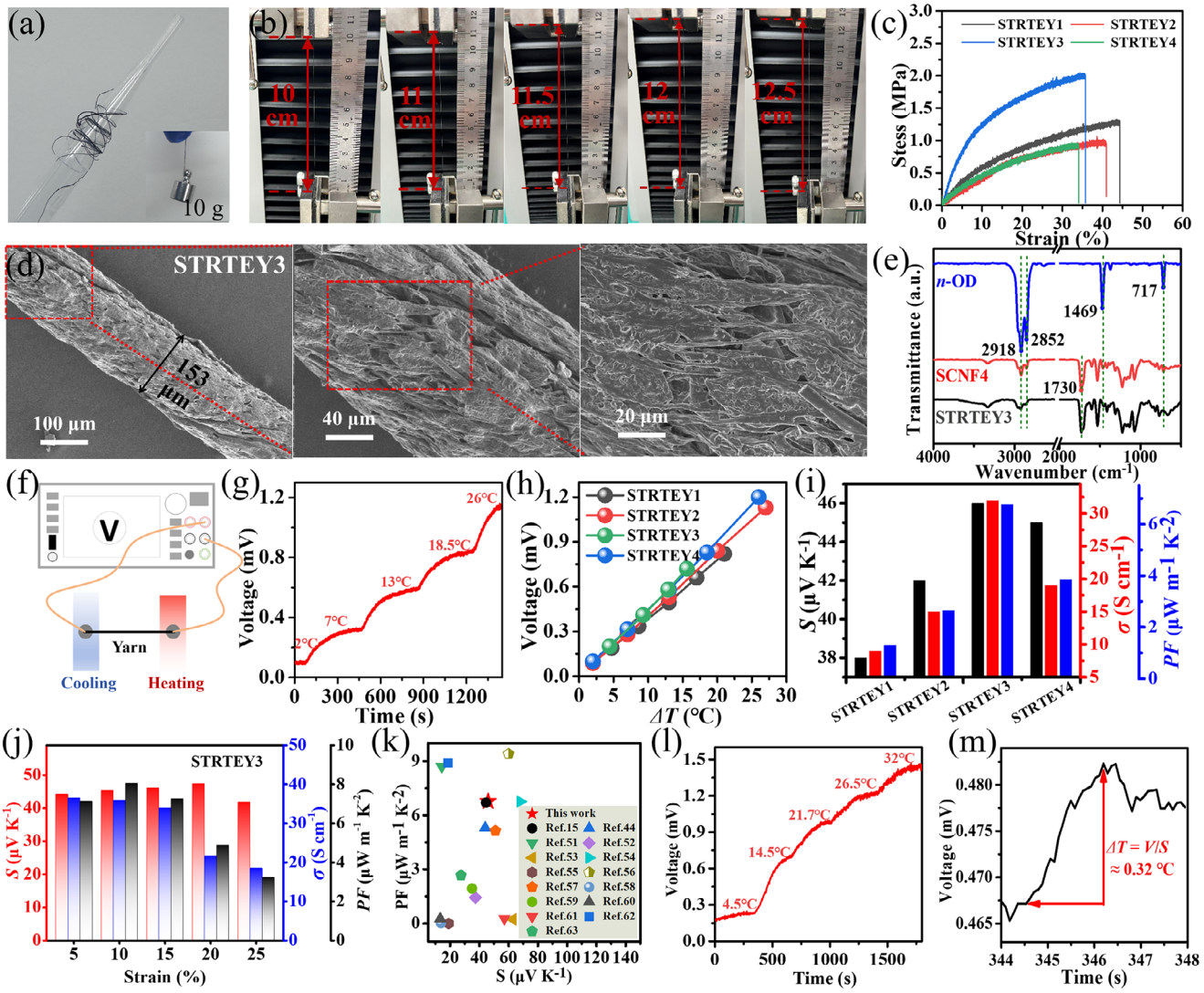

FIGURE 3 | Morphology, chemical and TE characteristics of STRTEYs. (a) Optical photograph of STRTEY3. (b) Optical images of the 10 cm-long STRTEY3 sample under different stretching states. (c) Stress-strain curves of STRTEYs with different SWCNT-to-PEDOT:PSS mass ratios. (d) SEM images of STRTEY3 at different magnifications. (e) FTIR spectra of *n*-OD, SCNF4 and STRTEY3. (f) Schematic diagram of TE test system. (g) The thermovoltage output response of the STRTEY3 under distinct temperature differentials. (h) The linear relationship between ΔT across the terminals of STRTEYs with different SWCNT-to-PEDOT:PSS mass ratios and the thermovoltage. (i) S, σ and PF of STRTEYs with different SWCNT-to-PEDOT:PSS mass ratios. (j) S, σ and PF of STRTEY3 under different stretching states. (k) Performance comparison between the STRTEY3 fabricated in this study and recently reported fiber-based stretchable thermoelectric devices. (l) The thermovoltage response of STRTEY3 under distinct temperature differentials following a 5-month storage period. (m) The minimum detectable temperature of the STRTEY3.

3.1 | Structure, Morphology, and Characteristics of SCNFs

As illustrated in Figure 2, we initially employed the facile coaxial electrospinning technique to fabricate PU/*n*-OD based SCNF samples. Systematic optimization and investigation were subsequently conducted focusing on the process parameters of their fabrication and the thermo-regulated performance of the resulting SCNFs. Figure 2a shows an optical photograph of SCNFs prepared via the scheme. It is evident that the SCNFs exhibit excellent flexibility, enabling effortless bending and flipping, which highlights their potential for application in wearable electronic devices. Figure 2b and Figure S1 depict the SEM surface morphologies of SCNFs prepared at different *n*-OD infusion rates, along with the corresponding diameter distributions of the shell-core nanofibers. At 0.5 mL/h and 0.7 mL/h infusion rates, the resulting SCNF1 and SCNF2 samples exhibited a certain number of spindle-shaped structures, indicating significant heterogeneity. As the infusion rate increased, the number of spindle-shaped structures in the SCNFs gradually decreased, and the fiber structures tended towards bead-free, straight, and cylindrical forms. Further analysis (Figure S1) revealed that the average diameter of SCNFs followed a trend of initial increase followed by decrease with increasing *n*-OD infusion rate, which was primarily attributed to viscosity and conductivity changes from *n*-OD loading. Among them, the SCNF4 sample prepared at an infusion rate of 1 mL/h had the largest fiber diameter (approximately 1.02 μm). Additionally, Figure 2c clearly illustrates the cross-sectional SEM micrograph of SCNF4, showing a distinct shell-core structure throughout the fiber, where the core

material (*n*-OD) was tightly encapsulated by the outer PU layer. This structure feature significantly ensures the thermo-regulated performance of the sample to a large extent. As displayed in Figure 2d, the FTIR spectra of all SCNFs exhibit characteristic peaks at 2920, 2852, 1470, and 717 cm^{-1}, corresponding to the -CH_3 and -CH_2 groups in *n*-OD [23, 43]. As the infusion rate of the *n*-OD increases, the intensity of these peaks follows a trend of initial increase followed by decrease, aligning with the above SEM results. Additionally, a strong absorption peak appears at 1730 cm^{-1}, attributed to the stretching vibration of imine bonds in PEI [44], thereby confirming the successful doping of PEI into the SNCFs.

Leveraging the latent heat storage/release properties of PCMs during quasi-isothermal transitions, PCM-integrated fibers/textiles retain intrinsic superiorities while enabling adaptive thermo-regulation and personalized thermal management. Thermal enthalpy and phase-transition temperatures are pivotal metrics for assessing thermal modulation capability [45]. As shown in Figure 2e, Figure S2 and Table S1, the DSC profiles of SCNFs exhibited distinct endothermic (melting) and exothermic (crystallization) peaks. Specifically, the melting enthalpy (ΔH_m) and crystallization enthalpy (ΔH_c) of the SCNF4 sample reach as high as 126.1 J/g and 125.3 J/g, respectively, indicating its exceptional thermo-regulated capability [46–48]. Consequently, all subsequent investigations will be conducted under the fabrication conditions optimized for SCNF4. Further analysis reveals that the onset melting ($T_{mo} \approx$ 26°C) and crystallization ($T_{co} \approx$ 25°C) temperatures align with human thermal comfort zone [23], thereby providing a platform for the development of wearable electronic devices integrating thermal comfort and showcasing broad application prospects in this domain.

Subsequently, a detailed characterization of the thermal stability of SCNF4 was conducted. As indicated by Figure 2f,g and Table S2, the DSC curves and FTIR spectra of SCNF4 remained largely unchanged after undergoing 100 thermal cycles, retaining a high enthalpy value and stable intrinsic chemical structure. Further analysis of Figure S3a revealed that the onset decomposition temperature of SCNF4 was approximately 140°C. These findings demonstrate that the SCNFs prepared in this study exhibit excellent thermal cycling stability and heat resistance, fully meeting the application requirements of human-wearable electronic devices. To more visually elucidate the thermo-regulated capability of SCNFs, multi-channel temperature logger and infrared thermal imager were employed to continuously monitor the temperature-time dynamic profiles of pure PU nanofiber film and SCNF4 during alternating exposure to high and low temperature environments. As illustrated in Figure 2h and Figure S3b, the temperature-time curves of SCNF4 exhibited remarkable consistency across 10 high-low temperature cycles. In comparison with the pure PU film, SCNF4 demonstrated pronounced latent heat storage and release plateaus, providing direct and compelling evidence of its exceptional thermal regulation efficiency. Furthermore, as shown in Figure 2i, the infrared thermal imaging revealed distinct color transition delays in SCNF4 during both heating and cooling processes, vividly illustrating its heat storage and release processes and underscoring its superior bidirectional temperature control performance. Notably, when subjected to low and high temperature conditions, SCNF4 outperformed the pure PU film in thermal insulation, achieving maximum heating and cooling capacities of 6.8°C and 4.0°C, respectively.

3.2 | Structure, Morphology, and Characteristics of STRTEYs

3.2.1 | Structure, Morphology, and Mechanical Characteristics of STRTEYs

The previous analysis indicates that the SNCF4 sample fabricated with both sheath and core infusion rates set at 1.0 mL/h demonstrates optimal thermo-regulated performance. Building upon these spinning parameters, a series of STRTEY samples were fabricated by adjusting the mass ratio of SWCNT-to-PEDOT:PSS in the coagulation bath (Figure 3a; and Figure S4). As illustrated in Figure 3a–c and Figure S5a, these STRTEYs exhibited exceptional flexibility, stretchability, weavability, and mechanical properties, with STRTEY3 demonstrating an elongation at break of 35% and a tensile strength of 2.00 MPa, while being capable of stably supporting weights approximately 7000 times its own mass. Further microscopic examination of the surface morphology (Figure 3d; Figure S4) and elemental mapping (Figure S6, where the presence and uniform distribution of S confirmed successful PEDOT:PSS doping) of STRTEYs revealed homogeneous deposition of TE components (SWCNT and PEDOT:PSS) on the yarn surface [49], accompanied by continuous fiber structures devoid of delamination defects. The cross-section SEM images (Figure S5b,c) reveal that STRTEYs exhibit a near-circular geometry and characteristic core-sheath porous structures formed by coaxial electrospinning, distinct from control sample. The FTIR spectra of STRTEYs, as shown in Figure 3e, displayed infrared absorption peaks corresponding to the *n*-OD core material, verifying the successful fabrication of core-sheath nanofiber-based thermal-regulated TE yarns via the coagulation bath-coaxial electrospinning approach. Further, the reduced intensity of characteristic FTIR peaks in STRTEY3 compared to SNCF4 film suggests lower encapsulation efficiency of *n*-OD within the yarn architecture, potentially compromising thermal management performance. Nevertheless, the developed STRTEYs retain exceptional phase-change thermo-regulated capability and PTM potential, as elaborated in subsequent sections.

3.2.2 | Thermoelectric and Thermo-Regulated Characteristics of STRTEYs

As illustrated in Figure 3f, this study systematically evaluated the TE performance of STRTEYs samples using a customized testing platform. Taking STRTEY3 as an example, a 10 cm-long yarn was connected in series with an LED bulb to form a closed-loop circuit, and the bulb successfully lit upon energization (Figure S5d), visually confirming the yarn's electrical conductivity. During testing, copper wire-yarn junctions were reinforced with silver conductive adhesive to eliminate contact resistance interference. The results (Figure 3g) demonstrate that the thermovoltage output of STRTEY3 increased linearly with rising temperature differentials. Based on the Seebeck coefficient calculation formula $S = \Delta V/\Delta T$, the Seebeck coefficient of the STRTEYs was derived (Figure 3h; Figure S7) [50], revealing that the mass ratio of SWCNT to PEDOT:PSS had a negligible impact on the Seebeck coefficient but a significant influence on

electrical conductivity, which exhibited a distinct ascending-then-descending trend with increasing SWCNT content (Figure 3i). This phenomenon can be attributed to the electrostatic self-assembly between cationic PEI in the PU sheath spinning solution and anionic PSS in the coagulation bath [44]. This interaction enhances the adsorption of TE materials onto the fiber surface, thereby optimizing conductive network formation. However, when SWCNT content exceeds a critical threshold, excessive SWCNTs aggregate, disrupting conductive pathways both on the yarn surface and within its interior, leading to a sharp decline in electrical conductivity. At the optimized mass ratio of SWCNT:PEDOT:PSS (6:4), the as-fabricated STRTEY3 achieved S, σ, and PF values of 46 μV/K, 32 S/cm, and 6.77 μW/(m·K^2), respectively, and maintained stable thermoelectric performance even when subjected to 15% mechanical deformation (Figure 3j; Figure S8), rendering it particularly well-suited for wearable electronic applications, significantly outperforming recent analogous studies (Figure 3k and Table S3) [15, 44, 51–63]. Notably, all constituent materials are commercially available at low cost (Table S4), ensuring both economic viability and scalability for potential mass production. Consequently, the as-fabricated STRTEY3 with this composition was selected for subsequent investigations. To validate yarn stability, aged STRTEY3 samples stored for five months were retested. The results (Figure 3l) revealed negligible thermovoltage output degradation and a stable S of 45.85 μV/K, demonstrating superior long-term durability fully compatible with the operational requirements of wearable electronic devices. Furthermore, as shown in Figure 3m, the STRTEY3 exhibits exceptional temperature responsiveness [57, 58], with a detection sensitivity for temperature differentials as low as 0.32°C, highlighting its significant application potential for self-powered temperature sensing and thermo-physiological monitoring.

Subsequently, based on the evaluation of the TE properties of STRTEYs, this study further systematically investigated their adaptive thermo-regulated performance and thermal stability, with a focus on evaluating the influence of the introduction of n-OD on the TE properties of the TE yarn while endowing it with PTM capability. As shown in Figure 4a,b, STRTEY3 exhibits superior phase-change thermo-regulated characteristic and thermal stability, with a thermal decomposition temperature reaching 170 °C. When fabricated under identical shell-core propulsion rates, the ΔH_m and ΔH_c of STRTEY3 show a marginal reduction compared to SCNF4, but still as high as 110.1 J/g and 108.7 J/g, far exceeding the reported values in recent analogous studies and the Grade 5A standard (72.0 J/g) specified in the industrial consortium guideline *T/GDBX 064—2023* for phase-change thermo-regulated fibers [46–48]. To directly validate its PTM performance, infrared thermography was employed to analyze its temperature-buffering capability under high-temperature and low-temperature conditions. As depicted in Figure 4c, STRTEY3 demonstrates pronounced thermal response lag during high-temperature heating and low-temperature cooling conditions, highlighting the effective regulation of temperature fluctuations by n-OD. Further, as displayed in Figure 4d,e, compared to pure PU yarn and control sample (TE yarn without PCM encapsulation), STRTEY3 exhibits superior thermal buffering performance, achieving peak temperature regulation differentials (cooling capacity) of 5.1 °C (vs. pure PU yarn) and 4.3 °C (vs. control yarn) under high-temperature conditions, as well as a insulation capacity of 5.1 °C (vs. pure PU yarn) and 4.7 °C (vs. control yarn) under low-temperature conditions, which validates its robust bidirectional temperature-control PTM functionality.

3.2.3 | Efficient Integration of Thermo-Regulated and TE Characteristics of STRTEYs

In this study, to precisely elucidate the efficient integration mechanism, the thermo-regulated and TE output characteristics of STRTEYs were simultaneously characterized using the experimental setup shown in Figure 4f. During the experiment, the T_c of the yarns was maintained constantly (approximately 15°C). The hot-side was placed on a hot plate to simulate a high-temperature environment and then transferred to a sealed ice bag to simulate a low-temperature environment. A multi-channel temperature recorder and a Keithley 2450 multimeter were used to continuously monitor and record the time-dependent variation curves of the T_h and thermovoltage for the control sample and the STRTEY3 sample (the results are shown in Figure 4g,h). Analysis revealed that, under the same test conditions, the hot-side heating rate of STRTEY3 was lower than that of the control sample, and the time required to reach the same set T_h was prolonged by approximately 40 s (Figure 4g). This phenomenon was mainly attributed to the latent heat storage associated with the solid-liquid phase-transition process of the phase change functional component in STRTEY3 upon heating. Further observation of Figure 4h showed that after the sample was transferred from the hot plate to the low-temperature environment, the T_h of the control sample dropped sharply, leading to a rapid decay in its thermovoltage output. In contrast, STRTEY3 benefited from the latent heat release and the resulting quasi-isothermal thermal buffering effect during the liquid-to-solid phase-transition of the phase change component. As a result, its thermal response was significantly delayed, and its T_h and thermovoltage remained significantly higher than those of the control sample during the cooling stage. Compared to control sample, the effective TE output duration of STRTEY3 in the low-temperature environment was extended by approximately 393 s, significantly enhancing the device's continuous power generation capability in a dynamic thermal environment. This experimental evidence demonstrates how PCMs fulfill their dual function in advanced PTM strategies: by leveraging adaptive latent heat storage and release, they stabilize the applied ΔT through quasi-isothermal thermal buffering while mitigating interfacial heat accumulation. In summary, the STRTEYs designed in this study exhibit excellent latent heat storage/release and thermal buffering properties, effectively maintaining the required temperature difference across the TEG device. This integrated approach not only ensures the long-term thermal comfort of wearable TEG devices but also improves the TE conversion efficiency by optimizing the stability of the temperature difference, achieving synergistic optimization of PTM and efficient TE energy harvesting, thereby addressing the critical trade-off between energy harvesting efficiency and thermal comfort in wearable applications.

3.3 | Application Explorations of STRTEYs

Leveraging the Seebeck effect of SWCNT and PEDOT:PSS within the STRTEYs framework, temperature differentials are directly

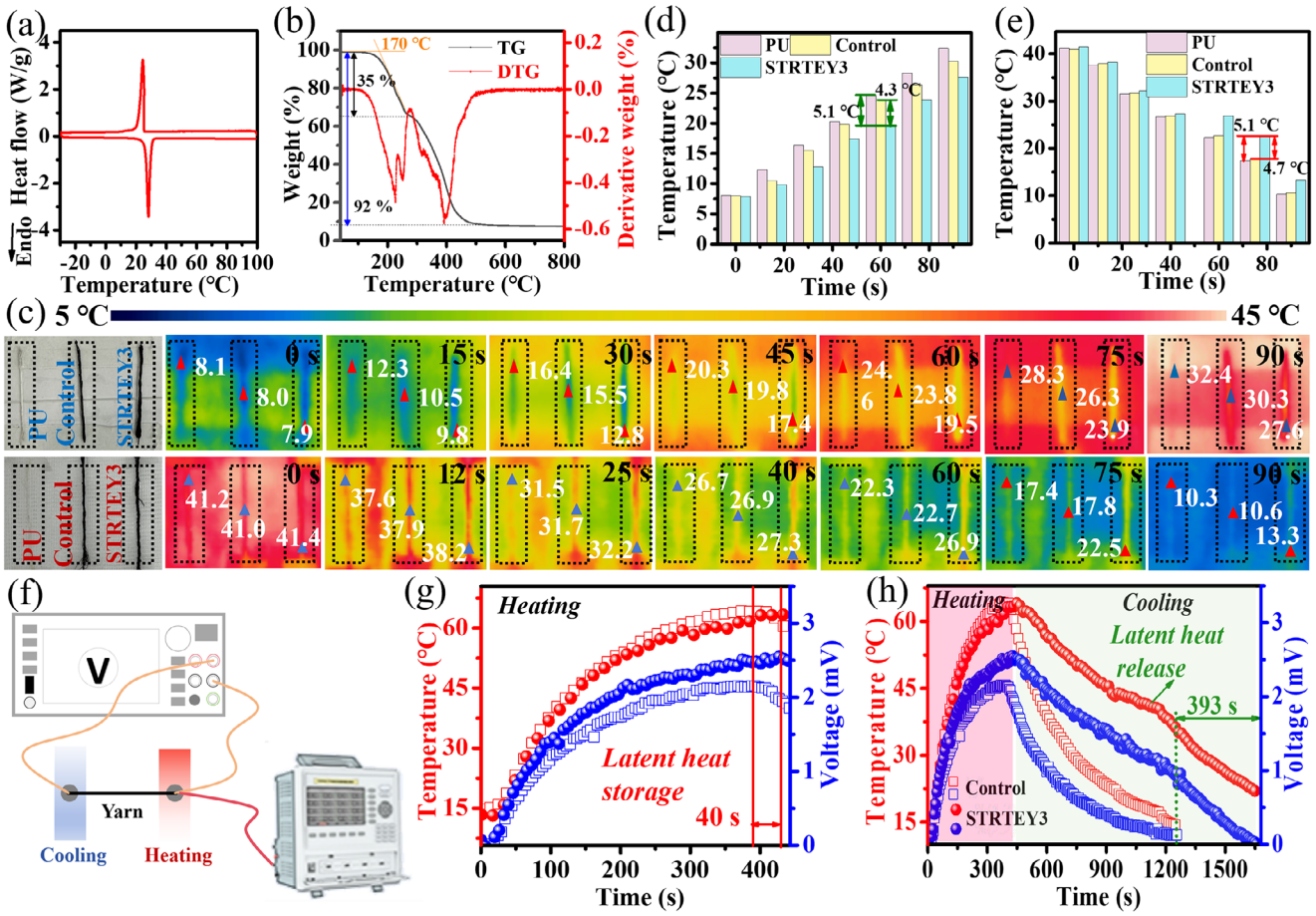

FIGURE 4 | Efficient integration of thermo-regulated and TE properties of STRTEYs. (a) DSC curve of STRTEY3. (b) TGA and DTG curves of STRTEY3. (c) Infrared thermal imaging images of PU, control sample of TE yarn without *n*-OD, and STRTEY3 exposed to high-temperature (up) and low-temperature (down) environments. Summary comparison chart of T_h for PU, control sample of TE yarn without *n*-OD, and STRTEY3 exposed to high-temperature (d) and low-temperature (e) environments. (f) Schematic diagram of the synchronous test system for thermo-regulated and TE characteristics. (g,h) Hot-side temperature/thermovoltage-time curves of control sample and STRTEY3 exposed to high-temperature and low-temperature environments.

converted into electrical signals. As illustrated in Figure 5a, through the physical bridging role of temperature, the system couples multimodal physiological signals to the thermoelectric conversion system, enabling self-powered sensing of physiological parameters such as core body temperature and respiratory rate. Furthermore, this technology is extended to smart textile applications, including self-powered wearable alert keyboards.

As depicted in Figure 5b, human exhaled heat during exercise generates temperature differentials with ambient air. By integrating STRTEYs into face masks, these differentials are converted into real-time thermovoltage signals for respiratory frequency monitoring, enabling health tracking. Analysis of the thermovoltage patterns reveals distinct correlations with physical activity: (1) During rest or slow walking, low and stable thermovoltages correspond to a calm breathing rhythm; (2) Initial high-intensity exercise leads to irregular breathing fluctuations, manifested as a disordered voltage trend (blue box). As rhythmic exercise stabilizes, the expansion of breathing amplitude and heat retention establish a stable thermal gradient, generating stronger periodic voltage outputs; (3) Irregular panting after exercise initially increases heat dissipation with each breath, creating a significant temperature difference, thereby sharply increasing voltage amplitude and fluctuation frequency (blue box). Subsequently, the regularization of breathing reduces voltage output because accelerated heat re-inhalation before full dissipation weakens the thermal gradient [64]. The data in Figure 5b unequivocally demonstrate that the self-powered STRTEYs integrated device precisely captures respiratory states (including depth and frequency) across activity dynamics, thereby offering a viable alternative approach for the realization of non-invasive health monitoring systems. As indicated in the preceding content (Figure 3j), STRTEYs exhibit an extremely high temperature sensitivity, enabling them to detect minute temperature fluctuations. Consequently, they are well-suited for use as electronic thermometers to monitor human body temperature in real-time and with high accuracy. As illustrated in Figure 5c, this study has integrated a STRTEY3 based temperature sensor into clothing near the chest or underarm area. When the human body temperature rises abnormally and exceeds the preset threshold, the sensor promptly issues a warning signal. Subsequently, we explored the application potential of STRTEYs in the realm of self-powered sensing. As illustrated in Figure 5d, four thermoelectric yarn-based temperature sensors with exceptional temperature

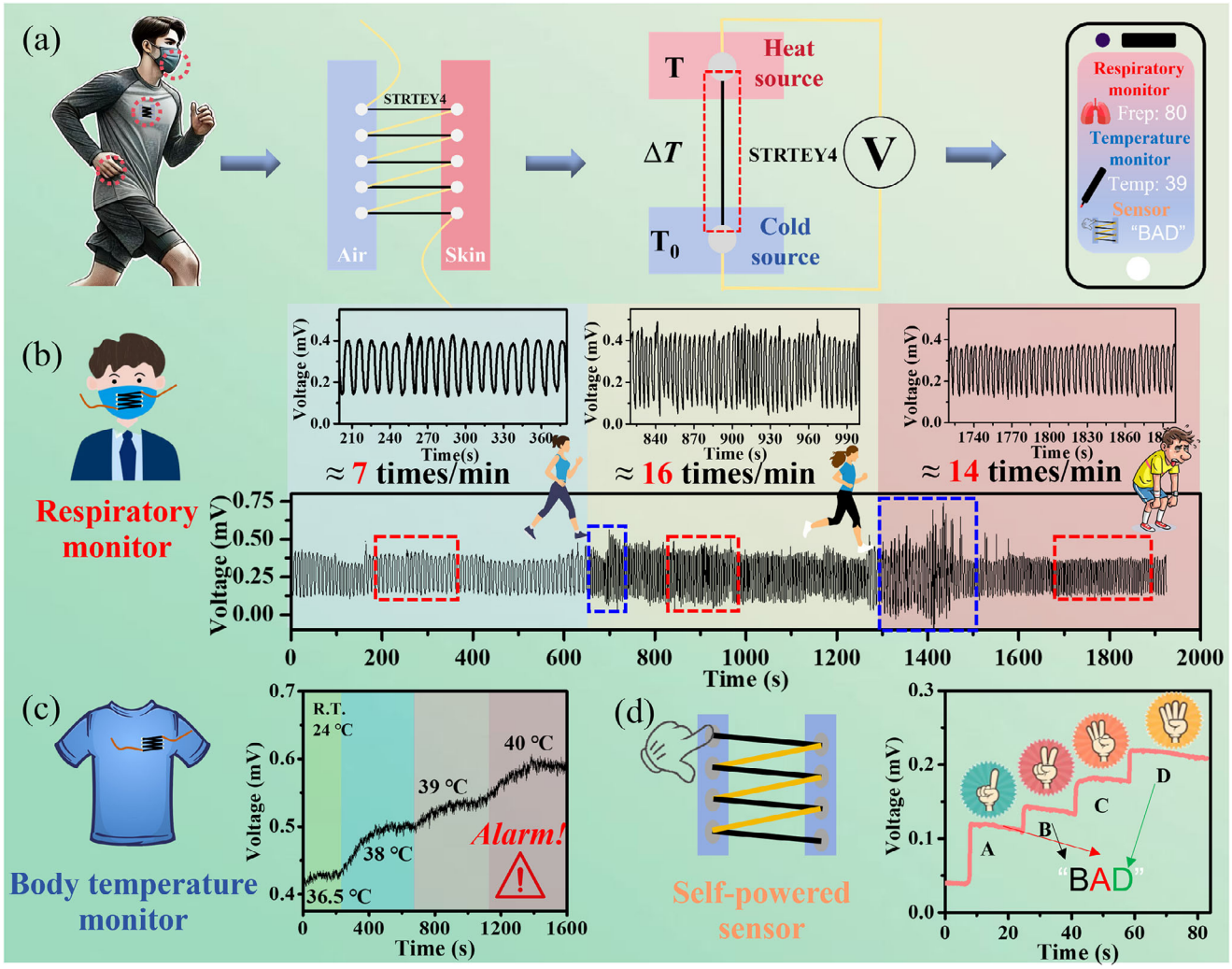

FIGURE 5 | Application explorations of STRTEYs. (a) Schematic diagram of wearable health monitoring system with integrated STRTEYs. (b) Self-powered respiratory monitoring mask for dynamic respiratory rate tracking across human multimodal exercise scenarios. (c) Schematic illustration and experimental validation of a self-powered body temperature monitoring system. (d) Schematic diagram and experimental demonstration of self-powered electronic keyboard.

sensitivity were seamlessly integrated into clothing. By modulating the number of fingers in contact (for touch interaction), we can transmit distinct temperature variations, which in turn generate thermovoltage signals of varying intensities. Building on this principle, thermovoltage signals of different intensities are artificially mapped to different letters or program activation buttons. With the help of diversified arrangements and combinations of these electrical signals, the specific needs of the wearer can be accurately met (Figure 5d). Moreover, the more thermoelectric yarns are incorporated, the broader the spectrum of functions that can be achieved, which will undoubtedly propel the wider adoption of thermoelectric devices in wearable electronic devices, such as self-powered flexible sensors and smart clothing.

4 | Conclusions

In this study, an innovative coagulation bath-integrated coaxial electrospinning technique was employed to successfully fabricate STRTEYs that exhibit high flexibility (>35%), excellent thermo-regulated performance ($\Delta H_m \approx 110.1$ J/g, $\Delta H_c \approx 108.7$ J/g), and enhanced TE characteristics (σ of 32 S/cm and S of 46 μV/K). Remarkably, the strategic incorporation of PCM enabled an exceptional extension of ≈393 s in effective TE output duration through efficient latent heat management, demonstrating unprecedented synergy between thermal regulation and energy harvesting. Crucially, after a long-term storage, the STRTEYs maintained stable TE property (with a S of 45.85 μV/K), providing a robust guarantee for their reliability in practical applications. Moreover, face masks and self-powered sensors integrated with STRTEYs enable self-powered real-time detection of physiological signals such as respiratory rate monitoring, and body temperature. The STRTEYs developed in this study have achieved efficient integration of multiple functions, including energy harvesting, adaptive personal thermal management, and self-powered sensing, which not only explores a brand-new direction for the research and development of cutting-edge multi-functional thermoelectric systems but also promotes their widespread application in self-powered flexible sensing devices, smart clothing and other wearable electronic devices.

Acknowledgements

This work was supported by the National Natural Science Foundation of China (Nos. 52003074, 52125205, U20A20166 and 52192614), Postdoctoral Fellowship Program of CPSF (No. GZC20230681), Fund of Key Laboratory of Advanced Materials of Ministry of Education (No. Advmat-2411), National key R&D program of China (No. 2024YFB3814104) and the Fundamental Research Funds for the Central Universities.

Conflicts of Interest

The authors declare no conflicts of interest.

Data Availability Statement

The data that support the findings of this study are available from the corresponding author upon reasonable request.

References

1. C. Li, D. Yang, Y. Liu, et al., "Optimizing Phase Change Heat Dissipation for Boosted Output Power and Wearing Comfort in Thermoelectric Generators," *Chemical Engineering Journal* 510 (2025): 161640, https://doi.org/10.1016/j.cej.2025.161640.

2. Q. Zhou, W. Xu, L. Wang, et al., "Triboelectric Nanogenerator-Based Self-Powered Urinary Protein Detection Utilizing Triboelectric Material With Colorimetric Function," *ACS Nano* 19 (2025): 1566–1576, https://doi.org/10.1021/acsnano.4c14800.

3. Y. Zhang, Q. Lu, J. He, et al., "Localizing Strain via Micro-Cage Structure for Stretchable Pressure Sensor Arrays with Ultralow Spatial Crosstalk," *Nature Communications* 14 (2023): 1252, https://doi.org/10.1038/s41467-023-36885-3.

4. Q. Chen, Q. Pan, S. Kang, et al., "Transparent Nanocrystal-in-Glass Composite Fibers for Multifunctional Temperature and Pressure Sensing," *Fundamental Research* 4 (2024): 624–634, https://doi.org/10.1016/j.fmre.2022.05.011.

5. Y. Xue, H. Jiang, P. Luo, et al., "Wearable Solar Ionic Thermoelectric Detectors for Human Motion Monitoring and Language Recognition Conversion," *Advanced Functional Materials* 35 (2025): 2422592, https://doi.org/10.1002/adfm.202422592.

6. Q. Huang, Y. Jiang, Z. Duan, et al., "Ion Gradient Induced Self-Powered Flexible Strain Sensor," *Nano Energy* 126 (2024): 109689, https://doi.org/10.1016/j.nanoen.2024.109689.

7. S. Zhang, X. Lin, J. Wan, C. Xu, and M. Han, "Recent Progress in Wearable Self-Powered Biomechanical Sensors: Mechanisms and Applications," *Advanced Materials Technologies* 9 (2024): 2301895, https://doi.org/10.1002/admt.202301895.

8. C. Zhang, X.-L. Shi, Q. Liu, and Z.-G. Chen, "Hydrogel-Based Functional Materials for Thermoelectric Applications: Progress and Perspectives," *Advanced Functional Materials* 34 (2024): 2410127, https://doi.org/10.1002/adfm.202410127.

9. J. Kim, S. Khan, P. Wu, et al., "Self-Charging Wearables for Continuous Health Monitoring," *Nano Energy* 79 (2021): 105419, https://doi.org/10.1016/j.nanoen.2020.105419.

10. J. Lv, X. Li, Z. An, et al., "Touch-Activated Information Interaction System Based on Body-Heat-Powered Flexible Thermoelectric Generator for Food Spoilage Monitoring," *Nano Energy* 123 (2024): 109418, https://doi.org/10.1016/j.nanoen.2024.109418.

11. J. Li, B. Xia, X. Xiao, et al., "Stretchable Thermoelectric Fibers With Three-Dimensional Interconnected Porous Network for Low-Grade Body Heat Energy Harvesting," *ACS Nano* 17 (2023): 19232–19241, https://doi.org/10.1021/acsnano.3c05797.

12. V. Karthikeyan, J. U. Surjadi, X. Li, et al., "Three Dimensional Architected Thermoelectric Devices with High Toughness and Power Conversion Efficiency," *Nature Communications* 14 (2023): 2069, https://doi.org/10.1038/s41467-023-37707-2.

13. J. P. Heremans and J. Martin, "Thermoelectric Measurements," *Nature Materials* 23 (2024): 18–19, https://doi.org/10.1038/s41563-023-01726-7.

14. C. Di, W. Xu, and D. Zhu, "Organic Thermoelectrics for Green Energy," *National Science Review* 3 (2016): 269–271, https://doi.org/10.1093/nsr/nww040.

15. H. Wang, K. Li, X. Hao, et al., "Capillary Compression Induced Outstanding n-Type Thermoelectric Power Factor in CNT Films Towards Intelligent Temperature Controller," *Nature Communications* 15 (2024): 5617, https://doi.org/10.1038/s41467-024-50057-x.

16. D. Zhang, Y. Fang, L. Liu, et al., "Boosting Thermoelectric Performance of Thermogalvanic Hydrogels by Structure Engineering Induced by Liquid Nitrogen Quenching," *Advanced Energy Materials* 14 (2024): 2303358, https://doi.org/10.1002/aenm.202303358.

17. J. Wang, Y. Song, F. Yu, et al., "Ultrastrong, Flexible Thermogalvanic Armor with a Carnot-Relative Efficiency Over 8%," *Nature Communications* 15 (2024): 6704, https://doi.org/10.1038/s41467-024-51002-8.

18. L. Miao, S. Zhu, C. Liu, et al., "Comfortable Wearable Thermoelectric Generator with High Output Power," *Nature Communications* 15 (2024): 8516, https://doi.org/10.1038/s41467-024-52841-1.

19. Y. Xu, B. Wu, C. Hou, Y. Li, H. Wang, and Q. Zhang, "Reconfigurable Flexible Thermoelectric Generators Based on All-Inorganic MXene/Bi_2Te_3 composite films," *FlexMat* 1 (2024): 248–257, https://doi.org/10.1002/flm2.28.

20. B. Wu, Y. Lin, Y. Tian, et al., "Bioinspired Wearable Thermoelectric Device Constructed With Soft-Rigid Assembly for Personal Thermal Management," *Advanced Functional Materials* 34 (2024): 2402319, https://doi.org/10.1002/adfm.202402319.

21. M. He, B. Zhao, X. Yue, Y. Chen, F. Qiu, and T. Zhang, "Infrared Radiative Modulating Textiles for Personal Thermal Management: Principle, Design and Application," *Nano Energy* 116 (2023): 108821, https://doi.org/10.1016/j.nanoen.2023.108821.

22. X. Li, W. Guo, and P. Hsu, "Personal Thermoregulation by Moisture-Engineered Materials," *Advanced Materials* 36 (2024): 2209825, https://doi.org/10.1002/adma.202209825.

23. Z. Zhu, A. Bashir, X. Wu, et al., "Highly Integrated Phase Change and Radiative Cooling Fiber Membrane for Adaptive Personal Thermal Regulation," *Advanced Functional Materials* 35 (2025): 2416111, https://doi.org/10.1002/adfm.202416111.

24. H. Liu, X. Zhang, S. Zhang, et al., "Intrinsically Flexible Phase Change Fibers for Intelligent Thermal Regulation," *Angewandte Chemie International Edition* 63 (2024): 202408857, https://doi.org/10.1002/anie.202408857.

25. M. Qin, Z. Shen, F. Xiong, S. Han, and R. Zou, "Toward High-Power and High-Density Thermal Storage: Dynamic Phase Change Materials," *ACS Energy Letters* 8 (2023): 3552–3557, https://doi.org/10.1021/acsenergylett.3c01222.

26. X. He, C. Fan, T. Xu, and X. Zhang, "Biospired Janus Silk E-Textiles With Wet–Thermal Comfort for Highly Efficient Biofluid Monitoring," *Nano Letters* 21 (2021): 8880–8887, https://doi.org/10.1021/acs.nanolett.1c03426.

27. J. Wang, L. Lu, K. Jiao, and M. Han, "Experimental Investigation of an Auto-Switching SH TEG/PCM Unit for Consistent All-Day Electric Power Generation," *Energy Conversion and Management* 327 (2025): 119556, https://doi.org/10.1016/j.enconman.2025.119556.

28. E. Yousefi, M. H. Kayhani, A. A. Nejad, and A. Nikkhoo, "Experimental Investigation of the External Load Effect on Thermoelectric Generator Discharge Time in a Low Power Energy Harvesting System," *Energy* 293 (2024): 130734.

29. X. Luo, Y. Cheng, Y. Liu, X. Xu, and Z. Tao, "Long-Term Energy Management Analysis of a Novel Solar Thermoelectric Generator

Based on Photothermal Conversion Phase Change Materials in Real-Environment," *Renewable Energy* 242 (2025): 122459.

30. Y. Kang, S. J. Lee, S. Kim, Y. Nam, and J. W. Jeong, "Performance Analysis of a Hybrid Energy Harvester Incorporating a Thermoelectric Generator and Phase-Change Material Through Annual Experiments," *Renewable Energy* 242 (2025): 122464, https://doi.org/10.1016/j.renene.2025.122464.

31. Y. Kang, P. Li, L. Liang, et al., "Integrated Thermoelectric Generation System for Sustainable All-Day Power Supply Based on Solar Energy and Radiative Cooling," *ACS Applied Materials & Interfaces* 17 (2025): 24030–24039, https://doi.org/10.1021/acsami.5c03010.

32. T. Yuan, J. Shang, H. Fang, H. Liu, and C. Bao, "A New Design of Extensible Solar-Driven Thermoelectric Array with Highly Thermo/Electro-Conductive PCMs as Solar Receivers, Thermal/Electric Bridges, and Voltage Fluctuation Suppressors Simultaneously," *Energy Conversion and Management* 252 (2022): 115079, https://doi.org/10.1016/j.enconman.2021.115079.

33. Y. He, Y. Wei, Y. Qian, et al., "A Flexible Phase Change Organohydrogel Created Using Pickering Emulsion Technology for Thermoelectric Conversion and Temperature Sensing," *Journal of Materials Chemistry A* 10 (2022): 18856–18865, https://doi.org/10.1039/D2TA04665B.

34. S. C. Yelishala, C. Murphy, and L. Cui, "Molecular Perspective and Engineering of Thermal Transport and Thermoelectricity in Polymers," *Journal of Materials Chemistry A* 12 (2024): 10614–10658, https://doi.org/10.1039/D3TA08071D.

35. J. F. Serrano-Claumarchirant, C. Cho, A. Cantarero, M. Culebras, R. Abargues, and C. M. Gómez, "How Plasmon Ag Nanoparticles can Enhance the Power Performance of a Thermoelectric Generator," *Small* 20 (2024): 2400345, https://doi.org/10.1002/smll.202400345.

36. C. Chen, F. Xu, Y. B. Wu, et al., "Manipulating Hetero-Nanowire Films for Flexible and Multifunctional Thermoelectric Devices," *Advanced Materials* 36 (2024): 2400020, https://doi.org/10.1002/adma.202400020.

37. Z. Luo, D. Yang, J. Liu, et al., "Nature-Inspired Solar-Thermal Gradient Reduced Graphene Oxide Aerogel-based Bilayer Phase Change Composites for Self-Adaptive Personal Thermal Management," *Advanced Functional Materials* 33 (2023): 2212032, https://doi.org/10.1002/adfm.202212032.

38. S. Fan, D. Guo, Y. Zhang, T. Chen, B. Li, and S. Zhang, "Washable and Stable Coaxial Electrospinning Fabric with Superior Electromagnetic Interference Shielding Performance for Multifunctional Electronics," *Chemical Engineering Journal* 488 (2024): 151051, https://doi.org/10.1016/j.cej.2024.151051.

39. Z. Li, L. Deng, H. Lv, et al., "Mechanically Robust and Flexible Films of Ionic Liquid-Modulated Polymer Thermoelectric Composites," *Advanced Functional Materials* 31 (2021): 2104836, https://doi.org/10.1002/adfm.202104836.

40. H. Li, Z. Ding, Q. Zhou, et al., "Harness High-Temperature Thermal Energy via Elastic Thermoelectric Aerogels," *Nano-Micro Letters* 16 (2024): 151, https://doi.org/10.1007/s40820-024-01370-z.

41. S. Zhang, H. Wang, J. Fu, and G. Chen, "Flexible Films of Poly(3,4-Ethylenedioxythiophene):Poly(Styrenesulfonate)/Single-Walled Carbon Nanotube/MXene Thermoelectric Composites and Their Devices," *Advanced Energy Materials* 6 (2025): 0143.

42. P. Fu, J.-K. Xiao, J.-Z. Gong, et al., "Interfacial Enhancement Effect of Graphene Quantum Dots on PEDOT:PSS/Single-Walled Carbon Nanotubes Thermoelectric Materials," *Synthetic Metals* 280 (2021): 116861, https://doi.org/10.1016/j.synthmet.2021.116861.

43. R. Cao, Y. Xia, J. Wang, et al., "Suppressing Thermal Negative Effect and Maintaining High-Temperature Steady Electrical Performance of Triboelectric Nanogenerators by Employing Phase Change Material," *ACS Applied Materials & Interfaces* 13 (2021): 41657–41668, https://doi.org/10.1021/acsami.1c11212.

44. X. He, J. Gu, Y. Hao, et al., "Continuous Manufacture of Stretchable and Integratable Thermoelectric Nanofiber Yarn for Human Body Energy Harvesting and Self-Powered Motion Detection," *Chemical Engineering Journal* 450 (2022): 137937, https://doi.org/10.1016/j.cej.2022.137937.

45. H. Liu, F. Zhou, X. Shi, et al., "A Thermoregulatory Flexible Phase Change Nonwoven for All-Season High-Efficiency Wearable Thermal Management," *Nano-Micro Letters* 15 (2023): 29, https://doi.org/10.1007/s40820-022-00991-6.

46. Y. Zhang, T. Li, S. Zhang, et al., "Room-Temperature, Energy Storage Textile with Multicore-Sheath Structure Obtained via in-Situ Coaxial Electrospinning," *Chemical Engineering Journal* 436 (2022): 135226, https://doi.org/10.1016/j.cej.2022.135226.

47. Y. Wang, J. Hu, Y. Jia, et al., "Nano-Structured Multicores-Sheath Thermoregulation Textile with Room Temperature Phase Change Point via Coaxial Electrospinning," *Journal of Energy Storage* 100 (2024): 113639, https://doi.org/10.1016/j.est.2024.113639.

48. Y. Lin, Q. Kang, Y. Liu, et al., "Flexible, Highly Thermally Conductive and Electrically Insulating Phase Change Materials for Advanced Thermal Management of 5G Base Stations and Thermoelectric Generators," *Nano-Micro Letters* 15 (2023): 31, https://doi.org/10.1007/s40820-022-01003-3.

49. J. Li, X. He, J. Wang, et al., "Nanoarchitectonics of High-Performance and Flexible n-Type Organic–Inorganic Composite Thermoelectric Fibers for Wearable Electronics," *ACS Nano* 19 (2025): 11440–11449, https://doi.org/10.1021/acsnano.5c01168.

50. Y. Qin, B. Qin, T. Hong, et al., "Grid-Plainification Enables Medium-Temperature PbSe Thermoelectrics to Cool Better Than Bi_2Te_3," *Science* 383 (2024): 1204–1209, https://doi.org/10.1126/science.adk9589.

51. L. Lu, Z. Liao, D. Xian, B. Zhao, C. Gao, and L. Wang, "Achieving High Thermoelectric, Stretchable, and Self-Healing Capabilities in Self-Supported PEDOT:PSS/Nafion/Poly(vinyl Alcohol) Composites for Wearable Thermoelectric Power Generators and Sensors," *ACS Applied Polymer Materials* 6 (2024): 14001–14008, https://doi.org/10.1021/acsapm.4c03143.

52. W. Jiang, T. Li, B. Hussain, et al., "Facile Fabrication of Cotton-Based Thermoelectric Yarns for the Construction of Textile Generator With High Performance in Human Heat Harvesting," *Advanced Fiber Materials* 5 (2023): 1725–1736, https://doi.org/10.1007/s42765-023-00305-4.

53. S. Liu, M. Zhang, J. Kong, H. Li, and C. He, "Flexible, Durable, Green Thermoelectric Composite Fabrics for Textile-Based Wearable Energy Harvesting and Self-Powered Sensing," *Composites Science and Technology* 243 (2023): 110245, https://doi.org/10.1016/j.compscitech.2023.110245.

54. T. Wei, H. Li, Y. Fu, X. Zheng, L. Huang, and A. Song, "A Graphene-Nanoribbon-Based Thermoelectric Generator," *Carbon* 210 (2023): 118053, https://doi.org/10.1016/j.carbon.2023.118053.

55. S. Xu, Z. Fan, S. Yang, et al. "Highly Flexible, Stretchable, and Self-Powered Strain-Temperature Dual Sensor Based on Free-Standing PEDOT:PSS/Carbon Nanocoils-Poly(vinyl) Alcohol Films," *ACS Sensors* 6 (2021): 1120.

56. G. Li, J. Zhou, L. Yang, Y. Deng, and Y. Wang, "A Highly Stretchable Thermoelectric Generator Developed from Polyaniline-Based Nanocomposites for Body Heat harvesting," *Journal of Materials Chemistry C* 13 (2025): 2295–2302, https://doi.org/10.1039/D4TC04252B.

57. X. He, J. Shi, Y. Hao, et al., "Highly Stretchable, Durable, and Breathable Thermoelectric Fabrics for Human Body Energy Harvesting and Sensing," *Carbon Energy* 4 (2022): 621–632, https://doi.org/10.1002/cey2.186.

58. Y. Cui, X. He, W. Liu, S. Zhu, M. Zhou, and Q. Wang, "Highly Stretchable, Sensitive, and Multifunctional Thermoelectric Fabric for Synergistic-Sensing Systems of Human Signal Monitoring," *Advanced Fiber Materials* 6 (2024): 170–180, https://doi.org/10.1007/s42765-023-00339-8.

59. X. He, J. Shi, Y. Hao, L. Wang, X. Qin, and J. Yu, "PEDOT:PSS/CNT Composites Based Ultra-Stretchable Thermoelectrics and Their

Application as Strain Sensors," *Composites Communications* 27 (2021): 100822, https://doi.org/10.1016/j.coco.2021.100822.

60. X. Zhang, B. C. Shiu, T. Li, et al., "Photo-Thermoelectric Nanofiber Film Based on the Synergy of Conjugated Polymer and Light Traps for the Solar-Energy Harvesting of Textile Solar Panel," *Solar Energy Materials and Solar Cells* 232 (2021): 111353, https://doi.org/10.1016/j.solmat.2021.111353.

61. B. Krause, C. Barbier, J. Levente, M. Klaus, and P. Pötschke, "Screening of Different Carbon Nanotubes in Melt-Mixed Polymer Composites With Different Polymer Matrices for Their Thermoelectrical Properties," *Journal of Composites Science* 3 (2019): 106, https://doi.org/10.3390/jcs3040106.

62. Y. Zhang, Y. Zhang, W. Deng, Q. Li, M. Guo, and G. Chen, "Skin-Like Soft Thermoelectric Composites With a "J-Shaped" Stress–Strain Behavior for Self-Powered Strain Sensing," *Advanced Functional Materials* 35 (2025): 2420644, https://doi.org/10.1002/adfm.202420644.

63. M. Li, H. Chen, J. Zhao, et al., "Stretchable Continuous p-n Alternating Thermoelectric Fibers for Energy Harvesting and Sensing Devices," *Advanced Composites and Hybrid Materials* 7 (2024): 106, https://doi.org/10.1007/s42114-024-00915-5.

64. P. Wang, G. Sun, S. Hua, et al., "Multifunctional All-Nanofiber Cloth Integrating Personal Health Monitoring and Thermal Regulation Capabilities," *InfoMat* 7 (2025): 12629.

Supporting Information

Additional supporting information can be found online in the Supporting Information section.

Supporting file 1: adfm73243-sup-0001-SuppMat.docx.

Supporting file 2: adfm73243-sup-0002-Video S1.mp4.